

Die Grenzen der
Chemie neu ausloten?
It takes
#HumanChemistry

Wir suchen kreative Chemikerinnen und Chemiker,
die mit uns gemeinsam neue Wege gehen wollen –
mit Fachwissen, Unternehmertum und Kreativität für
innovative Lösungen. Informieren Sie sich unter:

evonik.de/karriere

Elucidation of the Bulging Effect by an Improved Ray-Tracing Algorithm in Deep Penetration Wire Feed Laser Beam Welding and Its Influence on the Mixing Behavior

Marcel Bachmann,* Xiangmeng Meng, Antoni Artinov, and Michael Rethmeier

Herein, an improved ray-tracing routine using a virtual mesh refinement approach is adopted in a 3D transient multiphysics computational fluid dynamics model for deep penetration wire feed laser beam welding. In a previous study, it was shown that the improved localization of the reflection points of the subrays within the keyhole leads to a more realistic development of the keyhole depth being validated with experimental results. Another effect investigated in detail herein is a drastic change in the flow behavior in the weld pool, which promotes the occurrence of a necking area in the solidification line and subsequent bulging under specific circumstances. This has a detrimental effect on the filler material element transport in the weld pool, leading to an inhomogeneous dilution of the added material. The numerical observations are backed up by experimentally obtained data, allowing to provide a clear physics-based explanation of the reduced mixing behavior of the filler wire in the melt pool.

distortion. However, due to the use of small laser spot diameters with associated high energy density, this can lead to issues, for example, unmet assembly tolerances, limiting its practical application. Furthermore, elements with low boiling temperatures such as Mg or Zn may be lost due to the strong evaporation, thus being disadvantageous for the properties of the final weld.^[1]

A common approach to solve these kinds of issues is the use of filler wires during the LBW process known as wire feed LBW (WFLBW). The filler wire is melted by a part of the laser energy and then transfers to the molten pool.^[2] Thereby, the liquefied filler metal has larger dimensions compared with the laser spot and reduces the sensitivity of process instabilities due

1. Introduction and Motivation

In recent decades, laser beam welding (LBW), especially in the deep penetration mode, has attracted increasing attention. LBW offers some unique advantages, such as a precise and localized heat input, good penetration capability, and low residual


to gap misalignment or tolerances. Another advantage is the possibility to add alloying elements to the molten pool, which can take effect on metallurgical processes and the formation of possible defects, although this requires sufficient mixing in the weld pool. When the melt pool forms a narrow and deep geometry and high solidification rates occur, as often experienced in deep penetration LBW, the filler material cannot be transferred to the bottom of the melt pool. Instead, the filler wire material is concentrated in the top region of the weld, leading to inhomogeneous properties of the weld.^[3] The described effect becomes even more significant in partial penetration welding, where the weld pool is elongated in the surface-near region as a consequence of the action of the recoil pressure and Marangoni shear stress and becomes considerably shorter in the bottom region.^[4,5] A different type of weld pool geometry has also been observed, for example, in other studies,^[6,7] showing an elongated geometry both in the top and in the bottom region. Between these areas, the weld pool is remarkably narrowed. Under certain conditions, this region can also develop into a bulging region being characterized by an elongation of the solidification line.^[8] From this analysis, it is straightforward to assume that such narrow regions in the weld pool are detrimental to the homogeneity of mixing, especially during WFLBW, as this can interrupt the downward element transport being inserted at the top side of the weld pool.

Advances in numerical methods and in available computer power have paved the way for extensive numerical modeling for small-scale transient multiphysics processes like LBW.

M. Bachmann, X. Meng, A. Artinov, M. Rethmeier
Component Safety and Welding Technology
Bundesanstalt für Materialforschung und -prüfung (BAM)
Unter den Eichen 87, 12205 Berlin, Germany
E-mail: marcel.bachmann@bam.de

M. Rethmeier
Institute of Machine Tools and Factory Management
Technische Universität Berlin
Pascalstraße 8-9, 10587 Berlin, Germany

M. Rethmeier
Joining and Coating Technology
Fraunhofer Institute for Production Systems and Design Technology
Pascalstraße 8-9, 10587 Berlin, Germany

 The ORCID identification number(s) for the author(s) of this article can be found under <https://doi.org/10.1002/adem.202101299>.

© 2022 The Authors. Advanced Engineering Materials published by Wiley-VCH GmbH. This is an open access article under the terms of the Creative Commons Attribution License, which permits use, distribution and reproduction in any medium, provided the original work is properly cited.

DOI: 10.1002/adem.202101299

Where early numerical models focused exclusively on conduction welding^[9] involving only physical aspects with the highest significance,^[10] today's research in the welding field allows to accurately take into account different aspects of the beam–matter interaction, for example, multiple reflections of laser radiation, evaporation of the heated material, and deformation of the weld surface.

Subsequently, the improvements in the numerical framework nowadays allow for research of relevant aspects of academia and industry, such as pore formation or the hot cracking phenomena, which require a detailed description of the physical effects. Compared with simple heat conduction models,^[11,12] one of the first steps toward a more realistic 2D energy distribution in the keyhole in LBW was realized by the consideration of multiple reflections.^[13] More realistic models use ray-tracing algorithms in combination with tracking of the free surface by the volume-of-fluid (VOF) method^[14] or the level set method,^[15] allowing for transient calculation of the absorbed laser energy distribution at the keyhole wall. Depending on the research target, some of the models available in the literature include solid, liquid, and gaseous phases,^[16,17] whereas the gaseous phase is either neglected^[18,19] or considered by empirical equations in other studies.^[20,21] An analysis of the models available for LBW^[22] shows that an accurate temporal and spatial description of the energy coupling to the weld pool is crucial for reliable prediction of the behavior of the melt during the process and its solidification.

There to, it is shown in the study by Artinov et al.^[23] that for numerical models using the ray-tracing approach, a sufficient resolution of the keyhole region is essential for precisely localized energy absorption as this has a significant impact on the calculated penetration depth, especially for thick plate welding at higher processing speeds. Unfortunately, the computational capacity is often a limiting factor, and thus intermediate mesh sizes, for example, 0.2 mm in the study Cho et al.,^[24] which are in the order of the laser spot radius, are used. Motivated by this obvious issue, an improved ray-tracing algorithm using a virtual mesh refinement was implemented to calculate the reflection points of the single subrays of the laser radiation more accurately. In the study by Artinov et al.,^[23] this method was proposed for the precise calculation of the penetration depth and drilling speed. In the present study, it is shown that this method even shows major improvements in the accuracy of the melt flow behavior in the weld pool during investigations of the bulging effect also for lower welding speeds compared with a conventional ray-tracing approach.

2. Experimental Section

LBW experiments were conducted with AISI 304 stainless steel base metal and NiCr20Mo15 alloy filler wire, which allowed an evaluation of the stirring of the added material by their very different Ni contents. The weld specimen length was 200 mm, the width was 60 mm, and the thickness was 10 mm. The filler wire diameter was 1.1 mm. The experiments were done using an IPG YLR 20 000 laser system with a wavelength of 1.07 μm . The laser beam diameter in the focal plane was 560 μm . The focal plane was set at 3 mm below the top surface. A butt joint configuration

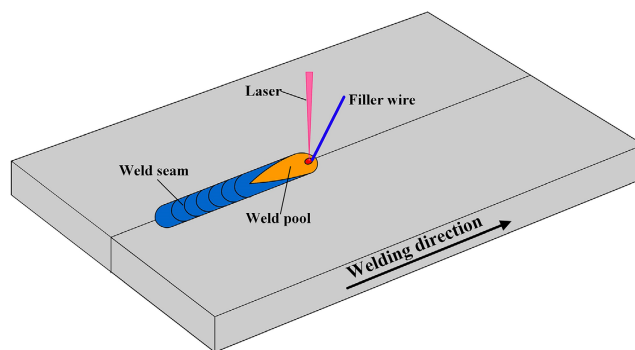


Figure 1. Sketch of the experimental setup.

with a technical zero gap was conducted. The laser head was fixed and aligned vertically to the weld specimen surface. A laser power of 6.5 kW and a welding speed of 1.3 m min^{-1} were utilized in the experiments. The filler wire was mounted in a leading position with a 33° angle to the surface and a feeding rate of 2.1 m min^{-1} was used. Argon shielding gas was provided with a flow rate of 20 l min^{-1} . A sketch of the experimental setup can be seen in **Figure 1**.

For metallographic postprocessing and analysis, transverse and longitudinal sections of the weld specimen were etched by a V2A etchant (100 mL H_2O , 100 mL HNO_3 , and 10 mL HCl) after mechanical cutting, grinding, and polishing. The mixing of the filler material with the base metal was characterized by ex situ X-ray fluorescence (XRF) element mapping with a scanning spot size of 20 μm and a measurement time per spot of 50 ms.

3. Numerical Modeling

3.1. General Assumptions and Equations

A 3D model coupled with the VOF algorithm^[25] allowing for the calculation of the element transport was developed. Temperature distributions, velocity fields, keyhole dynamics, and Ni distribution were calculated during WFLBW using a standard as well as an improved ray-tracing algorithm. The liquid metal and the gas were assumed to be Newtonian incompressible fluids, and the fluid flow regime was considered to be laminar. The equation system was solved by the universal CFD software ANSYS Fluent 19.5. The second-order upwind method was used for the spatial discretization of the convection–diffusion equations. The pressure-implicit with splitting of operators (PISO) algorithm was applied for pressure–velocity coupling. The convergence criteria of mass, momentum, energy, and Ni transport equations are 1×10^{-6} , 1×10^{-3} , 1×10^{-6} , and 1×10^{-3} , respectively. The typical time step size was $1 \times 10^{-6} \text{ s} - 1 \times 10^{-5} \text{ s}$. The calculations were performed on a high-performance computing cluster with 88 CPU cores and 768 GB RAM. The simulation time of one second of real-time welding was around 60 h.

The computational domain had the dimensions $30 \times 8 \times 12 \text{ mm}$. The mesh consisted of uniform hexahedral cells with a cell size of 0.2 mm in the welding zone, see **Figure 2**. An Eulerian reference frame was used. The laser beam and the filler wire were stationary

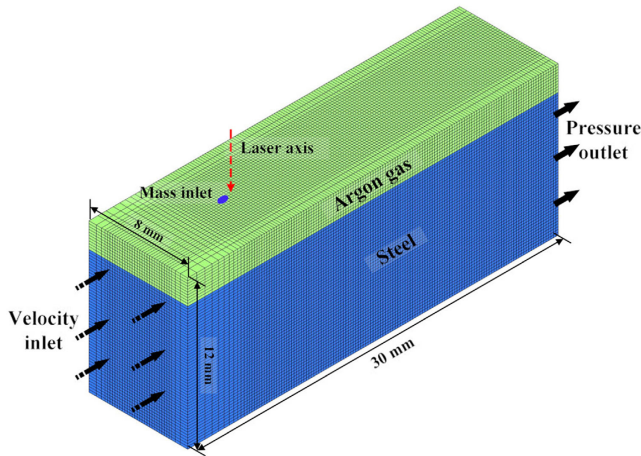


Figure 2. Computational domain.

during the simulation, and the workpiece was moved. The interaction between the laser beam and the solid filler wire was not simulated directly in the model. Instead, the temperature and velocity of the molten filler metal were taken from experimental^[26] and numerical studies.^[27] A mass inlet was set at the top of the simulation domain to realize filler metal transfer. The radius of the mass inlet of 0.3 mm was measured from high-speed images of the liquid bridge transfer of the wire to the weld pool. The detailed boundary conditions of the simulation domain are listed in **Table 1**.

Large parts of the model are based on previous studies of the authors. Therefore, only key features are presented here. Further details of the numerical model can be found in other studies.^[3,28–31] The main governing equations in a fixed Cartesian coordinate system are summarized.

Volume fraction conservation

$$\frac{\partial F}{\partial t} + \nabla \cdot (\mathbf{v}F) = S_F \quad (1)$$

Here, F denotes the volume fraction of the steel in a control volume, t is the time, and $\mathbf{v} = (v_x, v_y, v_z)$ is the fluid velocity vector. S_F includes the volume source caused by the added filler material. The free surface of the weld pool was reconstructed by piecewise linear interface calculation (PLIC).^[32]

Table 1. Energy and momentum boundary conditions.

	Energy	Momentum
Top surface	$T_w = 2900 \text{ K}$, if $r \leq 0.3 \text{ mm}$	$\mathbf{v}_w = 0.14 \text{ m s}^{-1}$, if $r \leq 0.3 \text{ mm}$
Side steel surface	Continuum boundary	$\mathbf{v} = 0$
Side gas surface	Adiabatic	Ambient pressure
Bottom surface	$k \partial T / \partial n = -h_c(T - T_0)$ $-\sigma \epsilon_r(T^4 - T_0^4)$	$\mathbf{v} = 0$

Mass conservation

$$\nabla \cdot \mathbf{v} = \frac{m_w}{\rho} \quad (2)$$

m_w denotes the added mass source term due to the filler material and ρ is the volume fraction averaged density depending on whether the simulation cell contains steel, air, or both.

Momentum conservation

$$\rho \left(\frac{\partial \mathbf{v}}{\partial t} + (\mathbf{v} \cdot \nabla) \mathbf{v} \right) = -\nabla p + \mu \nabla^2 \mathbf{v} - \mu K \mathbf{v} + m_w \mathbf{v}_w + \mathbf{S}_m \quad (3)$$

p is the fluid pressure, μ the volume fraction averaged dynamic viscosity, K is the Carman–Kozeny coefficient accounting for the deceleration of the melt in the mushy zone, and^[33,34] \mathbf{v}_w is the molten filler metal velocity. \mathbf{S}_m is the momentum source term taking into account the gravity term and buoyancy effects due to thermally induced variations of the metal density.^[35] As the free surface in the VOF method is not explicit, the effects of surface tension at the free surfaces,^[36] the recoil pressure,^[37] as well as empirical effects of the vapor on the keyhole surface^[20] were also implemented in \mathbf{S}_m . A detailed and complete description including all the assumptions and model equations not mentioned here can be found in the study by Artinov et al.^[31]

Energy conservation

$$\rho \left(\frac{\partial h}{\partial t} + (\mathbf{v} \cdot \nabla) h \right) = \nabla \cdot (k \nabla T) + h_w + S_q \quad (4)$$

Here h is the enthalpy, k is the heat conductivity, h_w is the energy source from the filler material, and S_q is an additional energy source term due to laser radiation as well as convective and radiative heat transfer, evaporation losses, and recondensation. The blocking effect of the filler wire on the laser beam energy distribution was considered empirically.^[38] Note that the attenuation of the laser radiation caused by the vapor plume was not considered in this study.^[39]

Element transport equation

$$\frac{\partial F \rho w_{Ni}}{\partial t} + \nabla \cdot (F \rho \mathbf{v} w_{Ni} - F D_{Ni} \nabla w_{Ni}) = S_{Ni} \quad (5)$$

w_{Ni} is the weight percentage of nickel, D_{Ni} is the diffusion coefficient of nickel in iron, and S_{Ni} is the source term due to the filler wire.

The material properties used in the calculations are average values depending on the mass fractions of the base metal and the filler metal. The values are given in **Table 2** and **Figure 3**.

3.2. Improved Ray-Tracing Routine

In CFD simulations of welding, a locally precise calculation of the laser beam absorption along the keyhole surface is essential for an accurate molten pool prediction. Therefore, standard ray-tracing algorithms are used for the calculation of multiple reflections of a sufficient number of subrays in the keyhole and Fresnel absorption.^[40] Each of the subrays has a location-dependent energy density and initial incidence angle. As the surface reconstruction algorithm of the VOF method leads to

Table 2. Thermophysical properties used in the simulations.^[45–47]

Property [unit]	Base metal AISI 304 steel	Filler wire NiCr20Mo15 alloy
Density [kg m ⁻³]	6900	8440
Thermal conductivity [W m·K ⁻¹]	T-dependent, see Figure 3	T-dependent, see Figure 3
Specific heat [J kg·K ⁻¹]	T-dependent, see Figure 3	575
Viscosity [Pa·s]	T-dependent, see Figure 3	T-dependent, see Figure 3
Surface tension coefficient [N m ⁻¹]	T-dependent, see Figure 3	–
Melting latent heat [kJ kg ⁻¹]	274	227
Liquidus temperature [K]	1727	1623
Solidus temperature [K]	1673	1563
Emissivity	0.4	0.4
Expansion coefficient [1/K]	1.2 × 10 ⁻⁵	1.6 × 10 ⁻⁵
Ni diffusion in iron [m ² s ⁻¹]	4.95 × 10 ⁻⁵	4.95 × 10 ⁻⁵

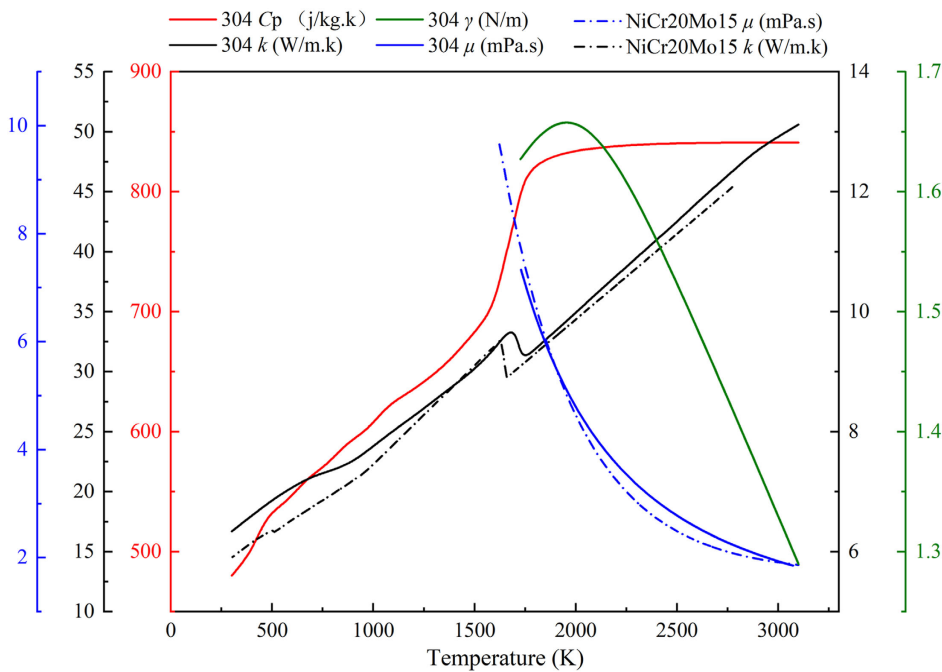


Figure 3. Thermophysical material properties used in the simulations.

a nonexplicit solution, the potential reflection cells for each of the subrays were identified when the following compromised search criterion was fulfilled.^[18]

$$D_{\text{ray}} \leq \frac{\sqrt{3}\Delta}{2} \quad (6)$$

where D_{ray} is the distance between the cell center and the incident ray and Δ is the cell size.

From the above criterion, issues in calculating the exact reflection points of the subrays can occur due to the direct influence of the cell size. Mesh sizes that are manageable from the point of view of computing time are in the order of magnitude of the laser spot diameter, which may lead to inaccurate locations of the

reflection points, for example, for typical keyhole front walls being almost parallel to the laser beam, see in **Figure 4a**.

An intuitive way to overcome this issue would be to reduce the mesh size, which results in a massive increase in computational costs. A smarter option to improve the model accuracy is a virtual mesh refinement of the identified reflection cells, thus keeping the computational effort almost constant,^[41] see **Figure 4b**. The virtual mesh refinement was conducted dynamically according to the transient keyhole geometry and the ray path. As a first step, the potential reflection cells were marked according to Equation (6) using Δ as the original cell size (0.2 mm). Then, these cells were refined virtually only for the calculation of the reflection points on the keyhole surface to a size of typically 0.05 mm. Then, the criterion shown in Equation (6) is repeated

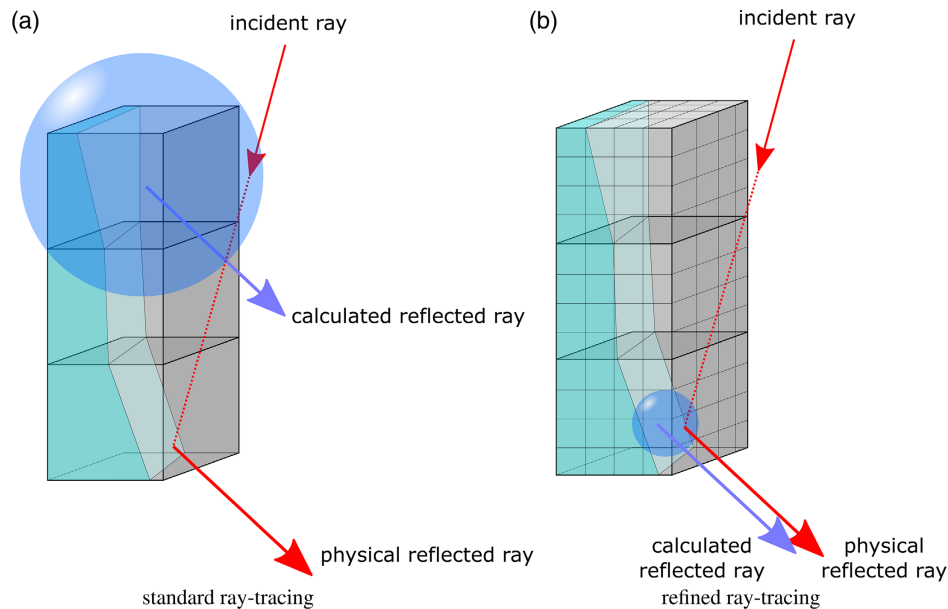


Figure 4. Standard ray tracing and improved ray tracing using a virtual grid refinement.

for all potential reflection points with a corresponding smaller Δ , thus improving the accuracy of the method. It should be noted that the virtual refinement algorithm does not belong to the mesh geometry and is only implemented in searching the potential reflection position. It is not involved in the mass and momentum equations and thus brings no additional iterative calculation.

4. Results and Discussions

As a first step toward the validation of the ray-tracing approach using a virtual mesh refining, two benchmark simulations were conducted. A series of keyhole geometries were randomly selected to evaluate the two ray-tracing algorithms, and an exemplary result is shown in **Figure 5**. The front wall of that geometry is steep and shows small humps, which can remarkably influence the reflection behavior of laser radiation. Without local mesh refinement (**Figure 5a**), the laser beam is absorbed punctually and hardly reaches the bottom region of the keyhole. Using the virtual mesh refinement to determine the reflection cells, the rays in **Figure 5b** reach the bottom of the keyhole, and the distribution of the laser energy is more widespread compared with the standard approach. Of course, the situation given in **Figure 5** only shows a single point in time during a calculation, but it indicates the advantages of the more sophisticated ray-tracing approach providing a better physical description of laser energy deposition on the keyhole wall. This is already shown to be critical for the accuracy of the simulated penetration depth, especially for welding speeds above $\approx 2 \text{ m min}^{-1}$, see the study by Artinov et al.^[23]

The comparison of the experimental and the numerical fusion lines for the standard ray tracing as well as the refined ray-tracing approach is shown in **Figure 6a**. The fusion lines from the experiments were taken from optical microscopy after cutting,

polishing, and etching the specimen, while the fusion lines from the simulations correspond to the maximum extent of the solidus isosurface along the simulated weld seam. One can see that both algorithms lead to energy deposition at the keyhole wall that allows for sufficient accuracy in the calculation of the weld cross section when compared with the experimental conditions in the relatively low welding speed range of 1.3 m min^{-1} . A preliminary experimental observation technique using a combination of metal and quartz glass in a butt joint configuration according to another study^[42] was used, allowing for optical observation of the weld pool from the side. It shows that narrowing of the weld pool in the longitudinal section and corresponding bulging in the lower part occur, which can neither be seen in the experimental cross sections nor the simulated ones, see **Figure 6a**. It is easy to see that such characteristics of the weld pool geometry during the welding procedure have a huge impact on the mixing behavior and the filler wire dilution.

Therefore, further model validation needs to be carried out by evaluating the nickel content in the longitudinal weld section, see **Figure 7**. The XRF results in **Figure 7a** show a distinct limit in the mixing depth of the added filler wire of $\approx 4 \text{ mm}$. In the upper part of the weld, the Ni content distribution is quite homogeneous around 20%, whereas it drops to a value of around 10% in the lower part. Here, the standard ray-tracing approach differs significantly, showing a more gradual decrease in Ni content with the depth starting at around 15% at the upper surface, down to around 12% at the weld pool bottom, see **Figure 7b**. In contrast, Ni distribution in the simulation using ray tracing with the virtually refined mesh presented in **Figure 7c** is very similar to the experimental observation with a relatively sharp decrease in Ni content at around the half weld pool depth dropping from around 20% down to 10% again, being in very good agreement with the XRF results. Note that the differences between the simulated and the experimentally obtained Ni distributions may be

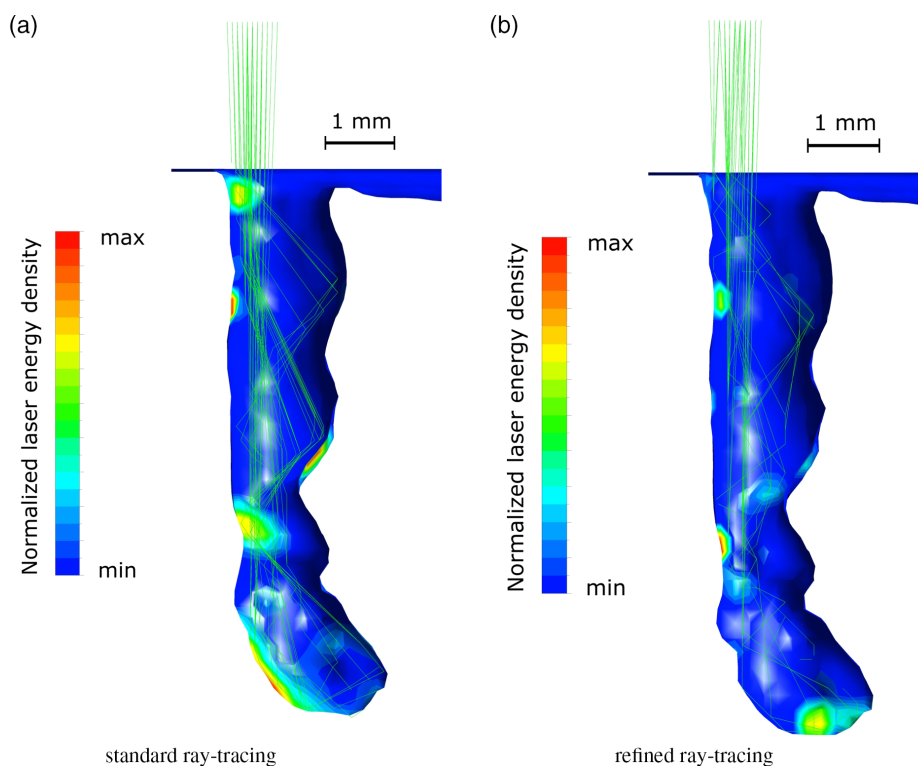


Figure 5. Comparison of the absorbed laser energy for the standard and the improved ray-tracing algorithm.

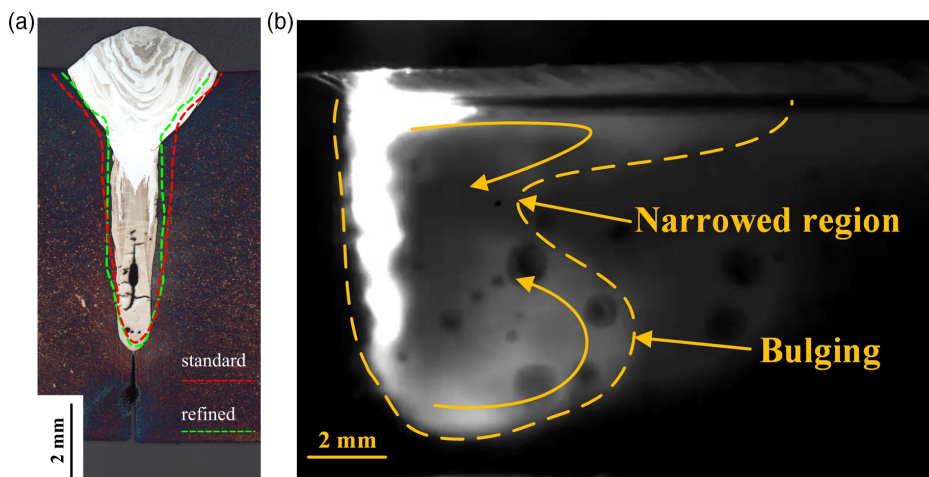


Figure 6. a) Comparison of the experimental and the numerical fusion lines for the standard ray-tracing and the refined ray-tracing approach. b) Weld pool dimensions in metal-glass observation experiments.

partly attributed to the fact that segregation during the solidification was not considered in the numerical model.

The reason for the changed Ni distributions in Figure 7b,c can be found in the flow field; see the temperature distribution and the velocity vectors for the standard ray-tracing approach in Figure 8a. Driven by the Marangoni forces and the recoil pressure, the melt is accelerated along the upper surface behind the keyhole. In the lower weld pool region, the main driving force is

only due to recoil pressure, which pushes the melt to the rear side locally at the points of the highest laser energy absorption depending on the calculated reflection points of the laser beam. Subsequently, the flow in the bottom region behind the keyhole is directed mainly against the welding direction first, later attaching to the solidification front at the weld pool rear side, forming a typical weld bead shape that is often seen in welding research with an elongated top side and being relatively

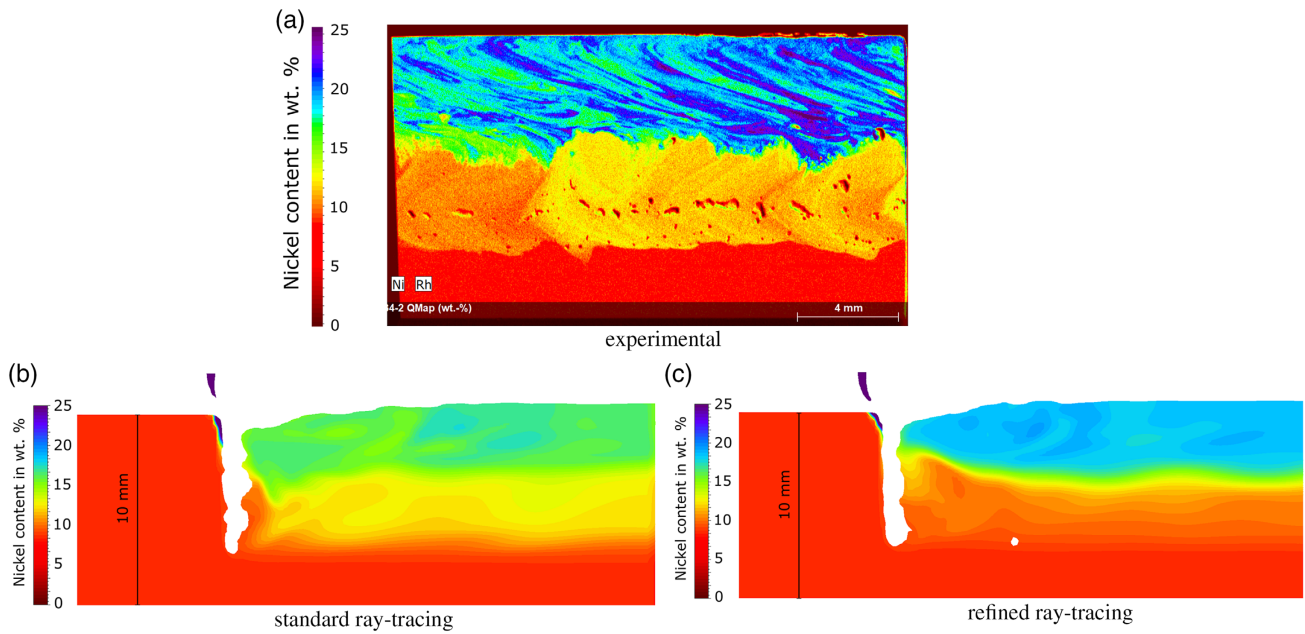


Figure 7. Comparison of the nickel distribution in experimental conditions and for the standard and the improved ray-tracing algorithm.

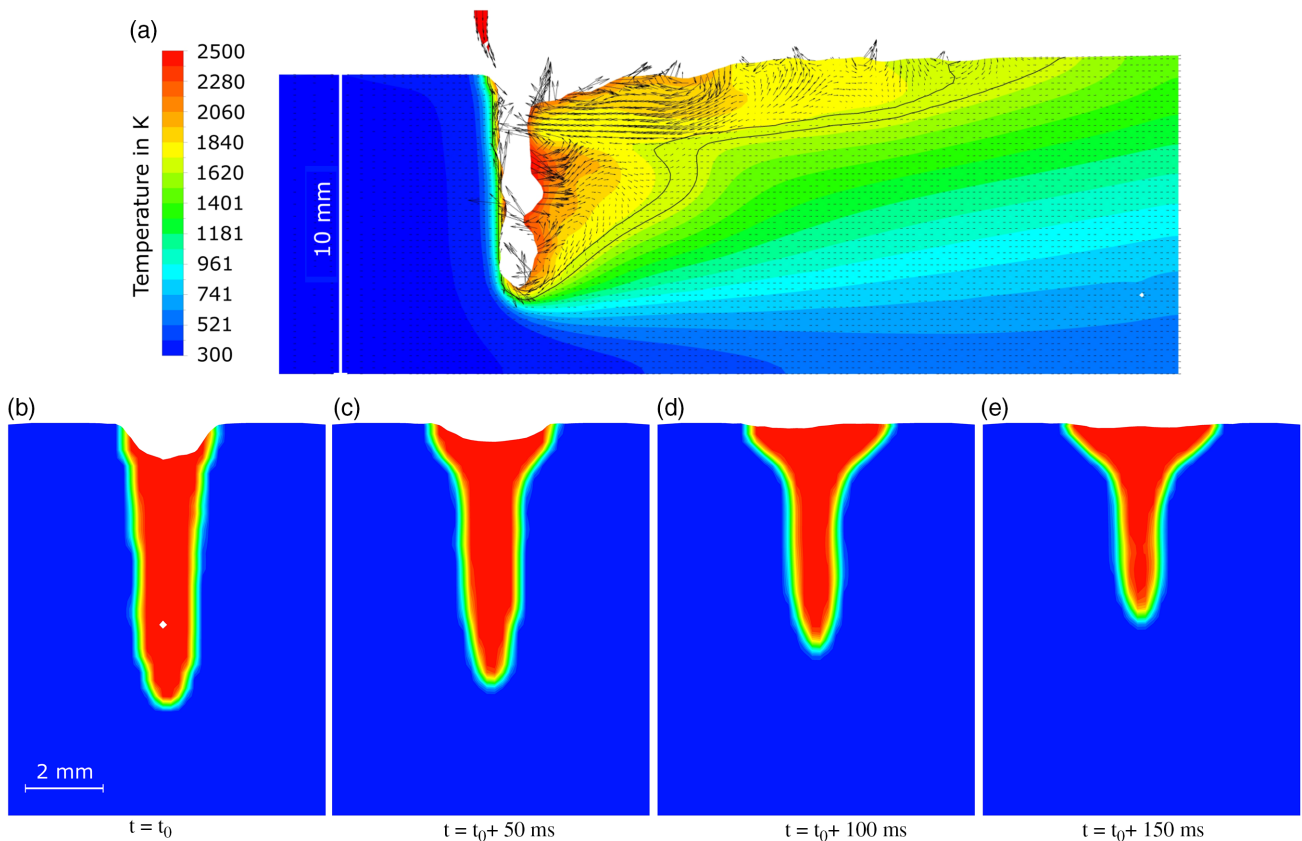


Figure 8. Standard ray-tracing approach. a) Weld pool temperature distribution and velocity vectors. b–e) Sequence of numerical weld cross sections during solidification. The data was extracted 2 mm behind the keyhole for different times.

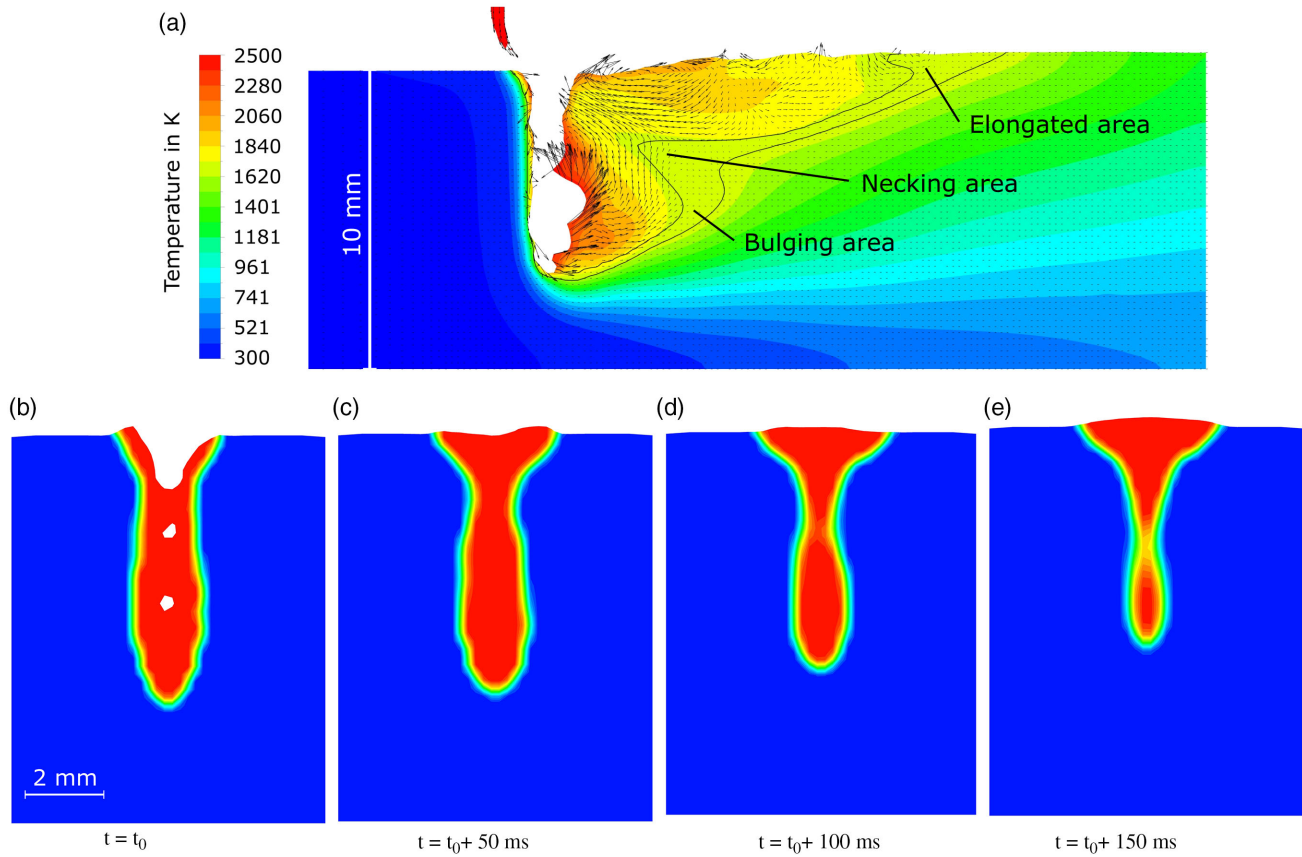


Figure 9. The refined ray-tracing approach. a) Weld pool temperature distribution and velocity vectors. b–e) Sequence of numerical weld cross sections during solidification. The data was extracted 2 mm behind the keyhole for different times.

shorter at the bottom.^[20,43] Nevertheless, the flow channel remains widely open to guarantee a potential mass exchange between upper- and lower-weld bead regions caused by transient fluctuations of the flow field. Hereto, the solidification sequence of the standard ray-tracing model can be seen in Figure 8b–e.

In contrast to the observed behavior of the standard ray-tracing model, the result of the improved ray-tracing routine is shown in Figure 9a. Although the physics involved forms a highly complex coupled and transient problem, a possible explanation for the observed behavior is the following. In comparison with Figure 8a, the more accurate calculation of the reflection points in the ray-tracing routine allows the rays to easily enter the lower part of the keyhole, see Figure 5b, resulting in more laser energy being deposited. This subsequently leads to an accumulation of higher recoil pressure in the depth of the keyhole. Thus, the liquid metal is pushed more strongly to the rear side of the weld pool. As the material contains and transports heat energy, the solidification line bends toward a convex shape, often referred to as bulge.^[44] This, in combination with the mass-conserving backflow of material that was originally accelerated along the upper surface, forms a narrow region between the vortex-dominated upper region of the weld pool and the bulging region. Similar behaviors can be seen in several different studies.^[8,21] Consequently, this narrow region has a detrimental effect

on the potential exchange of material between the upper part of the weld pool, where the filler wire is transferred to, and the base metal in the lower part. A sequence of such blocking effects by the separation of the different zones of the weld pool is shown in Figure 9b–e, leading to the bad mixing behavior here that was also found experimentally. In addition to previous studies with an improved ray-tracing formulation,^[23] an improvement here can clearly be seen for low welding speeds.

5. Conclusion

In this study, results of the multiphysical modeling of WFLBW and experimental research are presented. An improved ray-tracing algorithm was utilized, exploiting a virtual mesh refinement to improve the accuracy of the laser deposition in the keyhole. It could be shown that the occurrence of differently orientated vortices in the weld pool, as a consequence of the more accurately calculated energy deposition in the keyhole, leads to a phenomenon in the weld pool that forms a narrow region in its middle-thickness region. The formation of the separated zones is proven to be detrimental for homogeneous mixing of the added filler metal in the weld pool. The material, as well as energy transport, is blocked, leading to decoupling of the characteristics of the upper and lower weld bead regions. The

improvements in the numerical model were fundamental to provide a physics-based explanation for the separation zones in the weld bead and the observed insufficient mixing behavior.

Acknowledgements

This work was funded by the Deutsche Forschungsgemeinschaft (DFG, German Research Foundation)—project no. 411393804 (BA 5555/5-1) and no. 416014189 (BA 5555/6-1). This is dedicated to the 150-year anniversary of the Bundesanstalt für Materialforschung und -prüfung, Berlin, Germany.

Open access funding enabled and organized by Projekt DEAL.

Conflict of Interest

The authors declare no conflict of interest.

Data Availability Statement

The data that support the findings of this study are available from the corresponding author upon reasonable request.

Keywords

bulging effects, numerical welding simulations, ray-tracing methods, wire feed laser beam welding

Received: September 24, 2021

Revised: December 9, 2021

Published online:

- [1] U. Dilthey, A. Goumeniouk, V. Lopota, G. Turichin, E. Valdaitseva, *J. Phys. D: Appl. Phys.* **2000**, *34*, 81.
- [2] M. J. Torkamany, A. F. H. Kaplan, F. M. Ghaini, M. Vänskä, A. Salminen, K. Fahlström, J. Hedegård, *Opt. Laser Technol.* **2015**, *69*, 104.
- [3] X. Meng, A. Artinov, M. Bachmann, M. Rethmeier, *Proc. CIRP* **2020**, *94*, 722.
- [4] S. Katayama, Y. Kawahito, M. Mizutani, *Phys. Proc.* **2010**, *5*, 9.
- [5] Y. Kawahito, Y. Uemura, Y. Doi, M. Mizutani, K. Nishimoto, H. Kawakami, M. Tanaka, H. Fujii, K. Nakata, S. Katayama, *Weld. Int.* **2017**, *31*, 206.
- [6] H. Wang, M. Nakanishi, Y. Kawahito, *Opt. Express* **2018**, *26*, 6392.
- [7] M. Sohail, S.-W. Han, S.-J. Na, A. Gumenyuk, M. Rethmeier, *Int. J. Adv. Manuf. Tech.* **2015**, *80*, 931.
- [8] A. Artinov, N. Bakir, M. Bachmann, A. Gumenyuk, S.-J. Na, M. Rethmeier, *J. Laser Appl.* **2019**, *31*, 022413.
- [9] D. Rosenthal, *Weld. J.* **1941**, *20*, 220.
- [10] V. A. Karkhin, A. Y. Pilipenko, *Weld. Int.* **1997**, *11*, 401.
- [11] V. A. Karkhin, P. N. Homich, V. Michailov, *Math. Modell. Weld Phenom.* **2007**, *8*, 819.
- [12] J. R. Chukkan, M. Vasudevan, S. Muthukumar, R. R. Kumar, N. Chandrasekhar, *J. Mater. Process. Technol.* **2015**, *219*, 48.
- [13] A. F. H. Kaplan, *J. Phys. D: Appl. Phys.* **1994**, *27*, 1805.
- [14] J. Y. Lee, S. H. Ko, D. F. Farson, C. D. Yoo, *J. Phys. D: Appl. Phys.* **2002**, *35*, 1570.
- [15] S. Pang, W. Chen, W. Wang, *Metall. Mater. Trans. A* **2014**, *45*, 2808.
- [16] A. Otto, H. Koch, K.-H. Leitz, M. Schmidt, *Phys. Proc.* **2011**, *12*, 11.
- [17] W. Tan, N. S. Bailey, Y. C. Shin, *J. Phys. D: Appl. Phys.* **2013**, *46*, 055501.
- [18] J.-H. Cho, S.-J. Na, *J. Phys. D: Appl. Phys.* **2006**, *39*, 5372.
- [19] W.-I. Cho, S.-J. Na, M.-H. Cho, J.-S. Lee, *Comput. Mater. Sci.* **2010**, *49*, 792.
- [20] W.-I. Cho, S.-J. Na, C. Thomy, F. Vollertsen, *J. Mater. Process. Technol.* **2012**, *212*, 262.
- [21] S. Muhammad, S.-W. Han, S.-J. Na, A. Gumenyuk, M. Rethmeier, *J. Laser Appl.* **2018**, *30*, 012013.
- [22] J. Svenungsson, I. Choquet, A. F. H. Kaplan, *Phys. Proc.* **2015**, *78*, 182.
- [23] A. Artinov, X. Meng, M. Bachmann, M. Rethmeier, *Metals* **2021**, *11*, 8.
- [24] W.-I. Cho, S.-J. Na, *J. Weld. Join.* **2020**, *38*, 235.
- [25] C. W. Hirt, B. D. Nichols, *J. Comput. Phys.* **1981**, *39*, 201.
- [26] Y. Arata, H. Maruo, I. Miyamoto, R. Nishio, *Trans. JWRI* **1986**, *15*, 199.
- [27] R. Hu, M. Luo, T. Liu, L. Liang, A. Huang, D. Trushnikov, K. P. Karunakaran, S. Pang, *Sci. Technol. Weld. Join.* **2019**, *24*, 401.
- [28] X. Meng, M. Bachmann, A. Artinov, M. Rethmeier, *J. Manuf. Processes* **2019**, *45*, 408.
- [29] X. Meng, A. Artinov, M. Bachmann, M. Rethmeier, *J. Laser Appl.* **2020**, *32*, 022026.
- [30] X. Meng, A. Artinov, M. Bachmann, M. Rethmeier, *Int. J. Heat Mass Transfer* **2019**, *144*, 118663.
- [31] A. Artinov, X. Meng, M. Bachmann, M. Rethmeier, *Int. J. Heat Mass Transfer* **2021**, *184*, 122171.
- [32] D. L. Youngs, *At. Weapons Res. Establishment (AWRE) Tech. Rep.* **1984**, *44*, 35.
- [33] V. R. Voller, C. Prakash, *Int. J. Heat Mass Transfer* **1987**, *30*, 1709.
- [34] A. D. Brent, V. R. Voller, K. J. Reid, *Numer. Heat Transfer* **1988**, *13*, 297.
- [35] T. E. Faber, *Fluid Dynamics For Physicists*, Cambridge University Press, Cambridge **1995**.
- [36] K. C. Mills, B. J. Keene, R. F. Brooks, A. Shirali, *Philos. Trans. R. Soc. London Ser. A* **1998**, *356*, 911.
- [37] V. Semak, A. Matsunawa, *J. Phys. D: Appl. Phys.* **1997**, *30*, 2541.
- [38] X. Meng, M. Bachmann, A. Artinov, M. Rethmeier, *J. Mater. Process. Technol.* **2021**, *294*, 117135.
- [39] P. Y. Shcheglov, S. A. Uspenskiy, A. V. Gumenyuk, V. N. Petrovskiy, M. Rethmeier, V. M. Yermachenko, *Laser Phys. Lett.* **2011**, *8*, 475.
- [40] W. Schulz, G. Simon, H. M. Urbassek, I. Decker, *J. Phys. D: Appl. Phys.* **1987**, *20*, 481.
- [41] S.-W. Han, J. Ahn, S.-J. Na, *Weld. World* **2016**, *60*, 247.
- [42] Ö. Üstündag, N. Bakir, A. Gumenyuk, M. Rethmeier, *Opt. Laser Technol.* **2021**, *135*, 106715.
- [43] S. Pang, L. Chen, J. Zhou, Y. Yin, T. Chen, *J. Phys. D: Appl. Phys.* **2010**, *44*, 025301.
- [44] A. Artinov, M. Bachmann, X. Meng, V. Karkhin, M. Rethmeier, *Proc. CIRP* **2020**, *94*, 5.
- [45] D. Peckner, I. M. Bernstein, D. Peckner, *Handbook of Stainless Steels*, McGraw-Hill, New York, **1977**.
- [46] K. C. Mills, *Recommended Values of Thermophysical Properties For Selected Commercial Alloys*, Woodhead Publishing, Sawston **2002**.
- [47] K. D. Maglič, N. L. Perović, A. M. Stanimirović, *Int. J. Thermophys.* **1994**, *15*, 741.